https://dx.doi.org/10.1016/j.ymssp.2023.110999

Investigation on local monitoring paradigms of *in-situ* conformally fabricated piezopolymer coating-based array transducers: ultrasonic bulk waves and local ultrasonic resonances

Yehai LI[a,b,c], Zhijun YAO[a], Chao JIANG[a], Zhen ZHANG[e], Wei FENG[b,c], Zhongqing SU[f], and Shifeng GUO[a,b,c,d*]

[a]Shenzhen Key Laboratory of Smart Sensing and Intelligent Systems
Shenzhen Institute of Advanced Technology, Chinese Academy of Sciences, Shenzhen 518055, P.R. China

[b]Guangdong Provincial Key Lab of Robotics and Intelligent System
Shenzhen Institute of Advanced Technology, Chinese Academy of Sciences, Shenzhen 518055, P.R. China

[c]University of Chinese Academy of Sciences, Beijing 10049, P.R. China

[d]The Key Laboratory of Biomedical Imaging Science and System
Chinese Academy of Sciences, Shenzhen 518055, P.R. China

[e]School of Aerospace Engineering and Applied Mechanics
Tongji University, Shanghai 200092, P.R. China

[f]Department of Mechanical Engineering
The Hong Kong Polytechnic University, Hung Hom, Kowloon 999077, Hong Kong SAR

Submitted to *Mechanical Systems and Signal Processing*
(submitted on 10th August 2023, revised and re-submitted on 31st October 2023)

* To whom correspondence should be addressed. Email: sf.guo@siat.ac.cn

Abstract

Realistic structures with complex features have been intricate challenges for structural health monitoring (SHM) with permanently installed transducers. Poor conformability of conventional rigid and brittle piezoceramic wafers is a typical issue of applications on surfaces with complex geometry. Moreover, the accompanied high-stress concentration requires high-sensitivity defect detection which is difficult to achieve with large-area monitoring methods like lamb waves at tens to hundreds kHz. Previously *in-situ* conformally fabricated piezopolymer coating-based array transducers (PCATs) have been developed to build large-area, lightweight, flexible, and tunable Lamb wave networks. In this study, two novel local monitoring methods were investigated with PCATs, namely ultrasonic bulk wave array inspection and local ultrasonic resonance spectroscopy. For thick structures, ultrasonic bulk waves were generated and detected by PCATs with broadband operating frequencies (1-10MHz) and flexible array parameters. Simulation tools and imaging algorithms of array inspection in non-destructive testing (NDT) were well implemented based on the analogous directivity pattern and normal-pressure coupling mechanism. As proof of concept, PCATs were applied on example structures with flat, concave, and convex surfaces for internal defect imaging. For thin-walled and/or multilayer structures, PCATs were used to measure local ultrasonic resonances, comparable to conventional non-contact methods. With negligible influence on local mechanical properties and broadband frequency response, multiple resonance peaks from 0-25MHz were identified as zero group velocity (ZGV) Lamb modes and thickness vibration modes of host structures, which can be used as damage indices for local monitoring of corrosion, delamination, stiffness degradation, *etc*. Through embracing advanced NDT techniques with PCATs, high-sensitivity and quantitative local monitoring could be achieved with conformal networks, offering the possibility to integrate with large-area monitoring as multi-scale SHM for complex structures.

Keywords**:** structural health monitoring; piezopolymer coating; sensing network; ultrasonic wave; ultrasonic resonance; local monitoring

1. Introduction

Structural health monitoring (SHM) systems acquire and analyze data from permanently attached transducers to evaluate the integrity of structures, combined with instrumentations and algorithms. Successful SHM requires damage detection techniques that can cover a large region of structures, while inevitably losing sensitivity to a certain level. An extreme category is referred to global monitoring [1, 2], using vibration methods (also known as modal analysis) to achieve the whole structure coverage. However, it is insensitive to localized damage unless of significant severity, and thus generally associated with structural identification. Guided wave methods with an area monitoring capability, on the other hand, can detect localized damage using spatially distributed transducers. They utilize the guided nature of elastic waves propagating in the in-plane direction of the structures and are categorized as large-area monitoring [1, 3], based on area coverage much greater than the dimension of the applied transducers. However, suffering from the trade-off between area coverage and sensitivity, its defect detection capability still cannot compete with the advanced non-destructive testing (NDT) techniques, *e.g.* ultrasonic array inspection using bulk waves, even with complicated algorithms [4, 5]. Moreover, since guided wave propagation characteristics can be complicated by the localized structural complexity (involving features like stiffeners, multilayers, large curvatures, *etc.*) besides damages of the inspected structure, the application of guided wave techniques is often limited to simple (typically flat and uniform) structures which cannot be transferred directly to realistic structures like airframes [6]. However, considering common industrial applications, failure is likely to initiate within localized areas subject to high-stress concentration due to change in geometry, fastening, bonding, *etc.* Thus, routine NDT inspection is required in these areas but can only be performed when the structure is offline or undergoing maintenance.

Fortunately, the positions of these “hotspots” are generally known in advance in practical structures. Thus, high-sensitivity local SHM techniques offer potential solutions for these critical featured regions, with online and condition-based monitoring methods. Generally, such local monitoring was proposed to be complementary to global and large-area monitoring with fixed point transducers [7]. This category includes techniques that can only detect damages within a limited area around the spot of the applied transducers. Typical methods are comparative vacuum monitoring (CVM) [8], electro-mechanical impedance (EMI) [9], and intelligent coating monitoring (ICM) [10]. Although these methods have high sensitivity to small damages like cracks, they are usually difficult to provide quantitative evaluation, and additional different types of instrumentations and systems are required which could further increase the on-board burden.

Meanwhile, increasing attention has been drawn to converting advanced ultrasonic NDT methods to SHM, aiming to combine the merits of NDT (high sensitivity in localized areas) and SHM (without accessibility limitation or disassembly requirement). For example, ultrasonic array inspection using bulk waves is a popular routine NDT approach in many industrial scenarios to provide high-resolution images of defects which are often easy to interpret [11, 12]. It is a local inspection method based on the transmission and reflection of ultrasonic bulk waves in the local thickness direction of the structures. Many defect imaging algorithms have been developed to generate high-resolution images, such as the synthetic aperture focusing technique (SAFT) [13] and the total focusing method (TFM) [14, 15]. However, due to access requirements for operators to the structure, only routine inspections can be made when the structure is offline or undergoing maintenance. To adapt these ultrasonic NDT methods to the continuous and on-board local monitoring purpose of SHM, array transducers are one of the major concerns. Conventional ultrasonic array transducers

are made of compact multi-element piezoceramic or piezopolymer arrays between tailor-made backing and matching layers, then carefully packaged within a metal casing [16, 17], which result in high manufacturing cost, bulky size, and rigid contact (inaccessibility to curved or complicated surfaces), limiting the prospects of online SHM purposes. On the other hand, low-cost, low-profile, and lightweight transducers are always favored in the field of SHM [18-20], such as widely used piezoceramic wafers for ultrasonic guided waves [21]. After combing with flexible printed circuit (FPC) substrates, flexible networks could be realized on curved surfaces for large-area monitoring [22, 23]. Inspired by such a design, Sun *et al.* [24] developed a permanent ultrasonic bulk wave array transducer (multiple piezoceramic elements soldered to an FPC substrate) bonded onto curved-surface structures for continuous local damage monitoring. It should be noted that conventional planar fabrication methods of FPC substrate devices can yield flexible array transducers conformal to developable 2D curvilinear surfaces (*e.g.* cylindrical surfaces), but yet not conformal to non-developable 3D curvilinear surfaces (*e.g.* spherical surfaces). To achieve better conformability, stretchable ultrasonic bulk wave array transducers with 1–3 composite piezoceramic transducers and the "island-bridge" electrode layout were proposed with intimate contact on various complex surfaces such as pipeline elbows, wheel edges, and rail tracks [25]. However, complicated design and fabrication methods were required with multiple layers of different materials and sophisticated procedures.

Above mentioned newly-developed local monitoring methods mainly borrowed the idea from time-of-flight methods in ultrasonic NDT, with signal processing in the time domain. Thus, increasing wave frequency is necessary to improve detection sensitivity and avoid signal overlapping which often happens in thin-walled or multi-layer structures. However, strong signal attenuation is a serious problem encountered at high frequencies, especially in

composite materials. On the other hand, local ultrasonic resonance spectroscopy is a novel NDT method for damage detection and also material characterization [26-28]. Multiple resonance modes (*i.e.,* thickness-stretch vibration modes, thickness-shear vibration modes, and zero group velocity (ZGV) Lamb modes) can be extracted from the frequency spectrum, originating from the interference of multiple boundary reflection and mode conversion of elastic waves between top and bottom surfaces of the structures in the local thickness direction [29]. With advantages such as less attenuation, low frequency (wavelength of the order of plate thickness), and high sensitivity to local defects (*e.g.* debonding and corrosion) and changes in local mechanical properties (*e.g.* thickness and elasticity), local ultrasonic resonance spectroscopy is a promising local monitoring method to be developed for thin-walled and multi-layer structures, if a proper way of measurement can be found to meet SHM specifications. Unfortunately, in literature, these resonance modes were mostly generated and detected by lasers [30], electromagnetic transducers [31], and air-coupled transducers [32], due to their non-contact nature and broad frequency bandwidth excitation. Bonded piezoceramic wafers, on the other hand, were used in the EMI method to obtain local ultrasonic electro-mechanical resonances [33]. However, complicated electro-mechanical impedance modeling of coupled piezoceramic wafers and host structures makes it difficult to obtain quantitative interpretations of damage-related features from the frequency spectrum.

In the authors' previous work, piezopolymer coating-based array transducers (PCATs) were *in-situ* conformally fabricated on host structures for ultrasonic guided wave-based SHM as a large-area monitoring method, providing advantages such as lightweight, low profile, and flexibility [34]. In virtue of additive manufacturing technology, PCATs can easily conform to both developable and non-developable complex surfaces with straightforward

manufacturing processes. Moreover, by replacing costly and laborious manual installation, PCATs possess advantages such as high-production efficiency, high consistency, adhesive-free installation, and accurate position, compared to conventional piezoceramic wafer networks by human installation. Furthermore, thanks to the flexibility in designing electrodes, Lamb wave modes can be properly tuned by conveniently varying array parameters based on wavelength matching [35].

In this study, the applications of *in-situ* conformally fabricated PCATs for structural health monitoring are extended to local monitoring paradigms, by exploring the high-sensitivity damage detection possibility for critical or hotspot regions. Inspired by array inspection in ultrasonic NDT, ultrasonic bulk waves are transmitted and received for defect imaging in local thick hotspots. The electrical impedance measurement is implemented on a single PCAT element to verify its broadband frequency response, which indicates a flexible design strategy with operating frequency and array parameters for various inspection requests. The directivity of the single PCAT element is investigated theoretically and experimentally and proves the normal-pressure coupling mechanism between the PCAT and the host structure, which suggests the feasibility of using imaging algorithms and simulation tools of NDT array inspection. Simulation modeling is used to examine the TFM imaging algorithm and array design for internal defect imaging. According to simulation results, experimental verifications are conducted in block structures with flat, concave, and convex upper surfaces and artificial internal defects. For thin-walled or multilayer hotspots, local ultrasonic resonance spectroscopy is proposed as the local monitoring method with PCATs, which has high sensitivity within the low-frequency operating range. By comparing with PZT and noncontact laser, multiple modes including ZGV Lamb wave modes and thickness vibration modes are generated and detected with PCATs, thanks to the negligible influence on local

properties and broadband frequency response. These modes are directly associated with local thickness and elastic constants, which could be used as indices for damage detection. With high sensitivity, quantitative evaluation, and good conformability with complex surfaces, the proposed local monitoring methods can be used to be complementary to guided wave-based large-area monitoring on complex structures, especially for critical parts with complicated shapes. Moreover, local and large-area monitoring can be combined with PCATs using the same transduction system without other types of sensors or additional instruments.

2. Materials and fabrication

There is not much difference between the *in-situ* fabrication of PCATs for local monitoring in this study and for guided wave-based large-area monitoring previously. Therefore, only a brief description is presented here, while more details can be found in the authors' previous work [34]. PCATs are comprised of piezopolymer coatings as the function layer between the top and bottom electrode layers. If the host structure is intrinsically conductive like metals, it can be used as the bottom layer directly. PVDF-TrFE (Polyvinylidene fluoride copolymerized with trifluoroethylene) powder was selected as the raw functional material and obtained from Piezotech®, which was dissolved and spray coated directly onto surfaces of various host structures with a thickness of ~20μm. Annealing and corona poling were implemented to achieve the final piezoelectricity, with optimized processing conditions. Automated processes were realized with a precisely controlled robot arm. One difference should be mentioned that previously the electrode fingers of a PCAT were connected to build up a single actuator or receiver of guided waves with all array elements as a whole comb array transducer, thus mode control could be obtained by tuning array parameters [35]. In this study, the phased array design was used with each element working as an individual actuator or receiver of ultrasonic bulk waves or local ultrasonic resonances. Although the modality of PCAT is only slightly changed, the interrogating signals and capabilities are

quite different.

3. Local Monitoring using Ultrasonic Bulk Waves in Thick Structures

3.1. Principles and methods

An example is schematically shown in **Figure 1**. PCATs with linear-arrayed electrodes are *in-situ* conformally fabricated on the surface of the hotspot region of the structure where damages are prone to initiate. The Cartesian coordinate system is used. Array elements are determined by 1D linear-arrayed electrodes distributed in the x direction. Typically the element widths in the y direction are relatively long and thus infinitely long strip sources are assumed approximately in the modeling. Each array element will act in turn as the transmitter (T) of bulk waves propagating in the local thickness direction (z), while all array elements will act as receivers (R) of bulk waves reflected by boundaries and defects. With such a setting, data acquisition of full matrix capture (FMC) can be obtained from all combinations of transmitters and receivers.

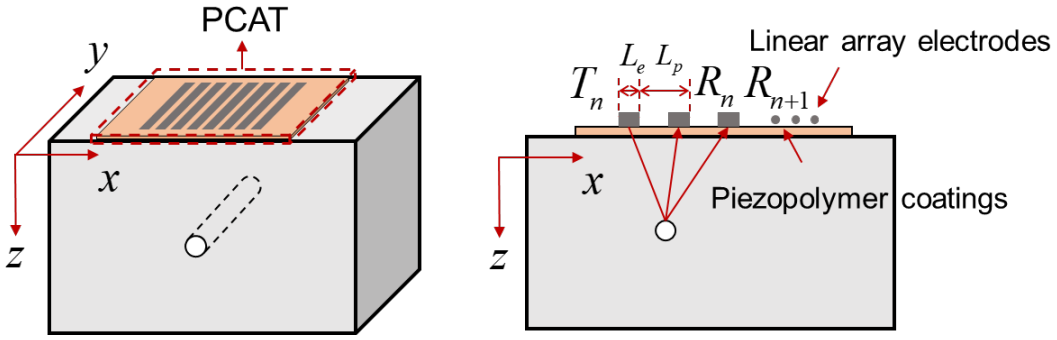

Figure 1. Schematics of ultrasonic bulk wave-based local monitoring with PCATs.

Then the 2D ultrasonic image is reconstructed in the x-z plane using the TFM imaging algorithm as

$$I(x,z)=\sum\left|H\left(f_{T_nR_n}(\Delta t)\right)\right|, \tag{1}$$

where $I(x,z)$ is the image pixel value at the focused spatial point (x,z). H is the energy envelope via Hilbert transform of the time-domain ultrasonic signal $f_{T_nR_n}(\Delta t)$ of the sensing

path from transmitter T_n to the receiver R_n. Δt corresponds to the travel time of waves forward from the transmitter $\left(x_n^T, z_n^T\right)$ to the focal point and backward to the receiver $\left(x_n^R, z_n^R\right)$ as

$$\Delta t\left(x,z\right)=\frac{\sqrt{(x-x_n^T)^2+(z-z_n^T)^2}+\sqrt{(x-x_n^R)^2+(z-z_n^R)^2}}{C}. \quad \textbf{(2)}$$

where C is the wave velocity. In this study, longitudinal waves are used solely for defect imaging, as prevalently used in ultrasonic NDT.

Array imaging performance is highly connected with the operating frequency and the applied array parameters (*i.e.*, element width L_e, inter-element pitch L_p, and element number of 1D linear arrays in this study). For example, element width and operating frequency determine the directivity of a single element, which is important for the detection of defects with large angles to the array center [36]. Moreover, minimizing the element width and inter-element pitch could improve image quality by suppressing artefacts (*e.g.* side lobes and grating lobes) [11]. Thus, in most commercial array transducers, the element length and inter-element pitch are required to be less than half a wavelength. With such limitations, larger array aperture can only be achieved by increasing the element number, for better resolution/sensitivity and larger coverage [37]. However, the acquisition and processing of FMC data with a dense array for TFM imaging are time-consuming, which could limit applications in some industrial fields, especially those with real-time requirements like SHM. Therefore, the sparse array pattern of fewer elements with relaxed requirements of element length and inter-element pitch was used when developing inspection modalities without using commercial array transducers [24, 25, 38-40]. Moreover, fewer transducer elements and larger coverage also fit the local monitoring purpose in this study, *i.e.*, typical sensor issues of SHM need to be concerned, *e.g.,* price, weight/volume penalty, and signal transmission [18]. To strike a

balance between “sensing cost” and “sensing effectiveness”, simulation tools are used to investigate array parameters and algorithms so that the required level of image quality can be achieved with an accepted level of artefacts, which have been proved as a key step in ultrasonic NDT [41].

3.2. Characterization of single element

3.2.1 Frequency response

Piezopolymer PVDF and its copolymer PVDF-TrFE with a small thickness and low modulus are proven to possess high resonance frequency and flat frequency response over a wide range of frequencies [17, 42]. Therefore, with the advantage of flexibility in designing electrodes of PCATs, guided waves could be conveniently tuned by demand in previous investigations for large-area structural health monitoring [35]. For local monitoring with ultrasonic bulk waves in this study, considering the various frequency requirements for different materials and defects of host structures, the broadband acoustic performance of PCATs is utilized with the operating frequency range below the first excitable resonance mode, which can be termed as non-resonant transducers [43-46]. Array parameters can then vary flexibly according to the selected operating frequency and required detection efficiency. The main disadvantage of non-resonant transducers compared to conventional resonant transducers is the small transmitted and received signal amplitudes. By virtue of the PCAT design, such a disadvantage could be reduced by direct contact with the host structure so that no attenuation is introduced by coupling agents or adhesives. Moreover, PCATs are backed only by air to further maximize the transmitted energy into the host structure.

To characterize the non-resonant range of PCATs, the frequency response was investigated using an impedance analyzer (HP 4294A, Keysight/Agilent). The electrical impedance

measurements were carried out on an 8-element PCAT with a thickness of 22μm *in-situ* fabricated on a rectangular block specimen as illustrated in **Figure 1**. From the results in **Figure 2**, the performance of elements was very consistent across the PCAT aperture, and the first resonant frequencies of four random elements were observed between 25.7-27.9MHz. According to the quarter-wavelength fundamental thickness mode of free-fix boundary conditions, the theoretical prediction is 27.0MHz ($2380 m \cdot s^{-1}/4 \times 22 \mu m$). It should be noted that conventional ultrasonic transducers utilize the half-wavelength fundamental thickness mode of free-free boundary conditions [44]. For further verification, a free-standing PCAT film was peeled off carefully from the attached structure, of which the corresponding resonant frequency is 52.0MHz (inset of **Figure 2**), approximately twice that of the attached PCAT. No other modes exit before the fundamental thickness mode in both attached and free-standing PCATs because of the large aspect ratio and/or restrained lateral and flexural vibration by the attached structure.

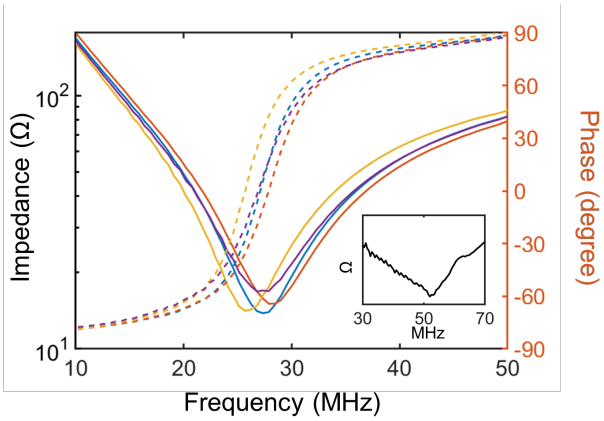

Figure 2. Measured electrical impedance (solid lines) and phase angle (dashed lines) of four random-picked PCAT elements on the host structure. Inset: electrical impedance of a free-standing PCAT film.

The broad bandwidth of PCATs ensures the non-resonant behavior within the typical frequency range (1-10MHz) of ultrasonic array inspection, which is not available with conventional resonant transducers and indicates versatile NDT applications. Moreover, the broadband response of PCATs also benefits the frequency-domain analysis which is the key

to developing local monitoring methods using local ultrasonic resonances in **Section 4**.

3.2.2 Directivity

The directivity function is used to describe the angular distribution of the radiated wavefield generated by a single element. For conventional array transducers in ultrasonic NDT, closed-form analytic solutions can be obtained by using the normal-pressure model to decouple the transducers and structures. In the case of the longitudinal waves in isotropic solids, the directivity function of a line source on the surface of a semi-infinite elastic solid can be written in polar coordinates as [11]:

$$D_L(\theta) = \frac{\cos\theta\left(\kappa^{-1} - 2\sin^2\theta\right)}{\left(2\sin^2\theta - \kappa^{-1}\right)^2 - 4\sin^2\theta\left(\sin^2\theta - 1\right)^{1/2}\left(\sin^2\theta - \kappa^{-1}\right)^{1/2}}, \quad \textbf{(3)}$$

where $\kappa = C_T^2 / C_L^2 = (1-2\upsilon)/2(1-\upsilon)$, with C_T and C_L the velocities of shear and longitudinal waves, and υ the Poisson ratio of the solid material. This function is for the line source of infinitesimal width, which is independent of wavenumber or frequency. For actual sources, the direction function requires further correction considering the finite size. For a strip-shaped source with finite width (L_e of linear PCATs in this study) in 2D modeling, the element aperture function Υ of wavenumber k is multiplied to obtain the corrected directivity function as

$$D(k,\theta) = D_L(\theta) \cdot \Upsilon(k,\theta), \quad \textbf{(4)}$$

where

$$\Upsilon(k,\theta) = \mathrm{sinc}\left(k\frac{L_e}{2}\sin\theta\right) = \mathrm{sinc}\left(\pi\frac{L_e}{\lambda}\sin\theta\right).$$
$$\mathrm{sinc}(x) = \sin(x)/x$$

Such element aperture function is also the directivity function of the radiated wavefield into the fluid. Using **Equation 4**, the relative amplitude of longitudinal waves with a specific ratio of element width to wavelength can be drawn with varying angles.

The directivity function of a single element is important and useful not only in forward wavefield modeling (*e.g.* beam profile modeling and point spread function) of array transducers [11, 15], but also in backward defect reconstruction (*e.g.* directional compensation) of array transducers [38]. To validate the above theoretical directivity function for PCATs, the directivity patterns of PCAT-generated longitudinal waves were measured experimentally. As illustrated in **Figure 3**, a single PCAT element (18mm×2mm) was fabricated on the flat surface of a half-cylinder aluminum specimen with a radius of 50mm and a width of 25mm. The large aspect ratio was selected to conform to the 2D assumption of plane waves. A high-power ultrasonic system (RITEC RAM-5000) was used to generate narrowband signals at certain center frequencies. A laser Doppler vibrometer (LDV, Polytec PSV-500) was used to measure the out-of-plane velocity on the arc surface at angles with respect to the middle plane. A rotating stage was used to facilitate the angular scanning. Experimental parameters are listed in **Table 1**.

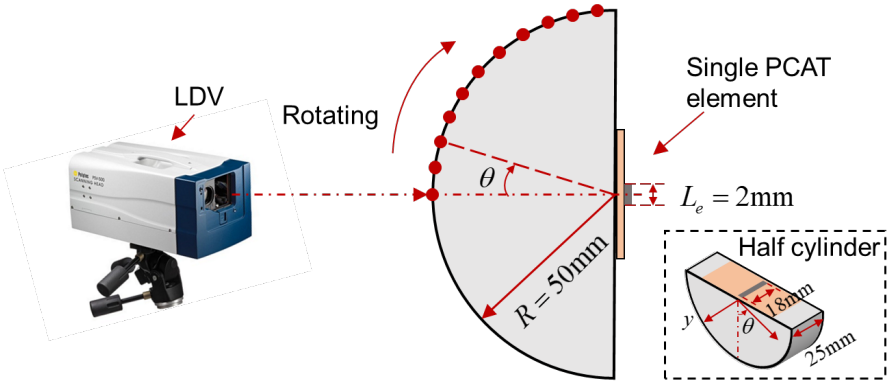

Figure 3. Experimental setups for directivity measurement of a single PCAT element.

Table 1
Experimental parameters for directivity measurement of a single PCAT element.

Parameter	Value
Excitation	5-cycle Hanning-windowed sinusoidal toneburst
Center frequencies f_c	2MHz, 5MHz, and 10MHz
Measurement	Out-of-plane velocity
Rotating angle θ	0° to 85° at step 5°

Experimental results are shown in **Figure 4**, with amplitudes normalized by the maximum value at θ=0°. Compared to the theoretical directivity function, experimental directivity has a similar shape of the main lobe but stronger side lobes. The reasons could be multifold: the real coupling mechanism could be more complicated than the simplified normal-pressure model; the toneburst excitation is of a certain frequency bandwidth rather than the continuous wave excitation of a single frequency in directivity function; the existence of 3D boundaries disrupts the assumed 2D wavefield. Nevertheless, the theoretical directivity function offers a good approximation especially for the main lobe or at low frequency where no side lobes exist, following a general trend that a small ratio of element width to wavelength yields wave radiation over a great angular region, while a large ratio produces a more directional wavefield. Therefore, the normal-pressure coupling mechanism is still valid for PCAT modelling, considering the large discrepancy between it and the shear-stress coupling [47], which is also consistent with the authors' previous study when investigating Lamb wavefields excited by PCATs [35]. In this study, the normal-pressure coupling mechanism was then used to simplify the simulation modeling of multi-element PCATs for defect imaging.

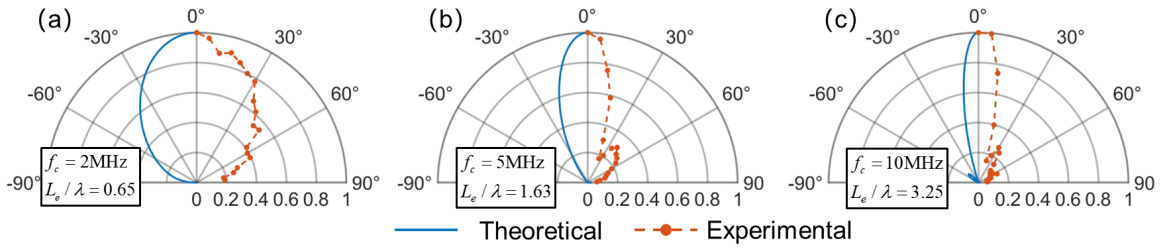

Figure 4. Polar plots of theoretical (blue solid line) and experimental (orange dashed line with dots) directivity of longitudinal waves at center frequencies of (a) 2MHz, (b) 5MHz, and (c) 10MHz.

3.3. Internal defect imaging with phased array

3.3.1 Simulation modeling

The simulated sample block for internal defect imaging is illustrated in **Figure 1**. The 2D model was built in COMSOL with a length of 60mm (*x* direction) and a thickness of 50mm (*z* direction). The simulated material was aluminum, with a longitudinal wave velocity of 6150m/s. Absorbing layers were added to the left and right boundaries to reduce the reflection. The analysis module was *Elastic Waves, Time Explicit*, with normal pressure applied along the upper surface covered by the transmitter element in turn. A side-drilled hole (SDH) defect of 2 mm diameter was placed at a depth of 25 mm (half thickness). Two different configurations of array parameters were investigated with similar array aperture sizes. Simulation parameters are listed in **Table 2**.

Table 2
Simulation parameters for internal defect imaging with PCATs.

Parameter	Value
Excitation	2-cycle Hanning-windowed sinusoidal toneburst
Center frequencies f_c	3MHz
8-element PCAT	2mm L_e, 3mm L_p, total 26mm aperture
16-element PCAT	1mm L_e, 1.5mm L_p, total 25mm aperture

Defect imaging results are shown in **Figure 5** using the TFM algorithm in **Equation 1** and **2**. For both cases, wave reflection from the defects and the bottom boundaries can be clearly identified, although the near-field blind zone is stronger with increased element number due to surface wave interference among elements. According to such simulation results, the 8-element PCAT is selected to identify the SDH defect in the experimental study.

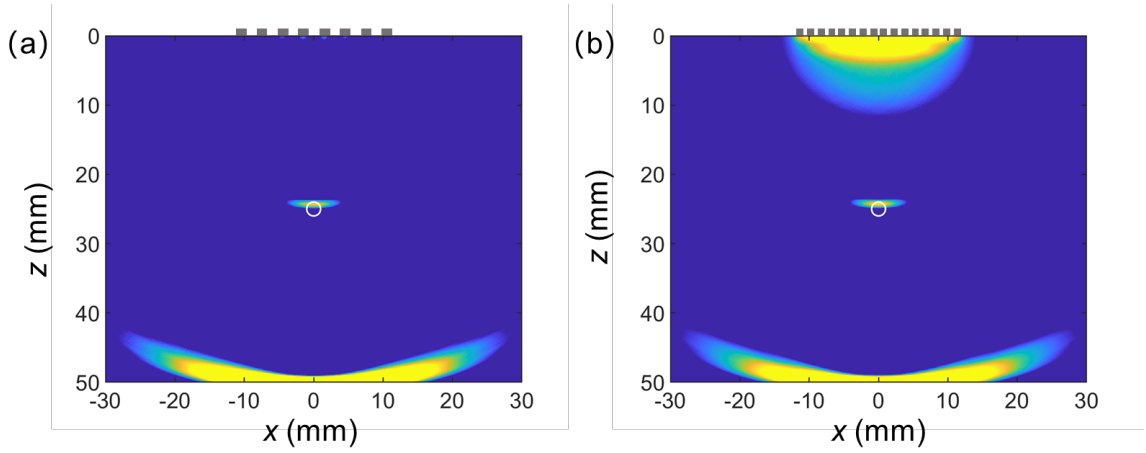

Figure 5. Simulated TFM images of SDH (white circled) with (a) 8-element PCAT and (b) 16-element PCAT.

3.3.2 Experimental verification

To verify the imaging performance of the selected PCAT, an aluminum block with a machined SDH and a flat upper surface was prepared of the same size as in the simulation model, except for the lateral size which was 100mm in *x* direction (**Figure 6a**). A 60mm×50mm region of interest (ROI, blue dashed rectangle) was set as the inspected area following the simulation model. An 8-element PCAT was fabricated on the upper surface and connected to a data acquisition system (DAQ) via copper wires soldered on printed electrodes. The DAQ consists of a multiplexing controller which is integrated on an NI (National Instruments) platform for switching from transmitter to receiver for each element, a high-power ultrasonic system (RITEC RAM-5000) with a signal generator and amplifier to apply excitation voltage (~300V_{pp}) on the transmitter, and an oscilloscope to acquire signals from the receiver. The array parameters and operating excitation were the same as in the simulation model. The experimental image result is shown in **Figure 6b**, which proves the local monitoring performance of PCATs using ultrasonic bulk waves. The near-field blind zone is stronger compared to simulation results in **Figure 5a** due to crosstalk caused by electromagnetic interference among elements at the initial time (excitation moment), which is not modeled in the simulation. Since the verified modeling and imaging methods are

identical to those used in ultrasonic array inspection with conventional array transducers, the imaging performance of PCATs can be further improved by many techniques including signal processing like filtering and gating, ameliorated TFM algorithms to reduce artefacts, *etc*., which have been well studied in vast NDT literature and will not be covered in this study.

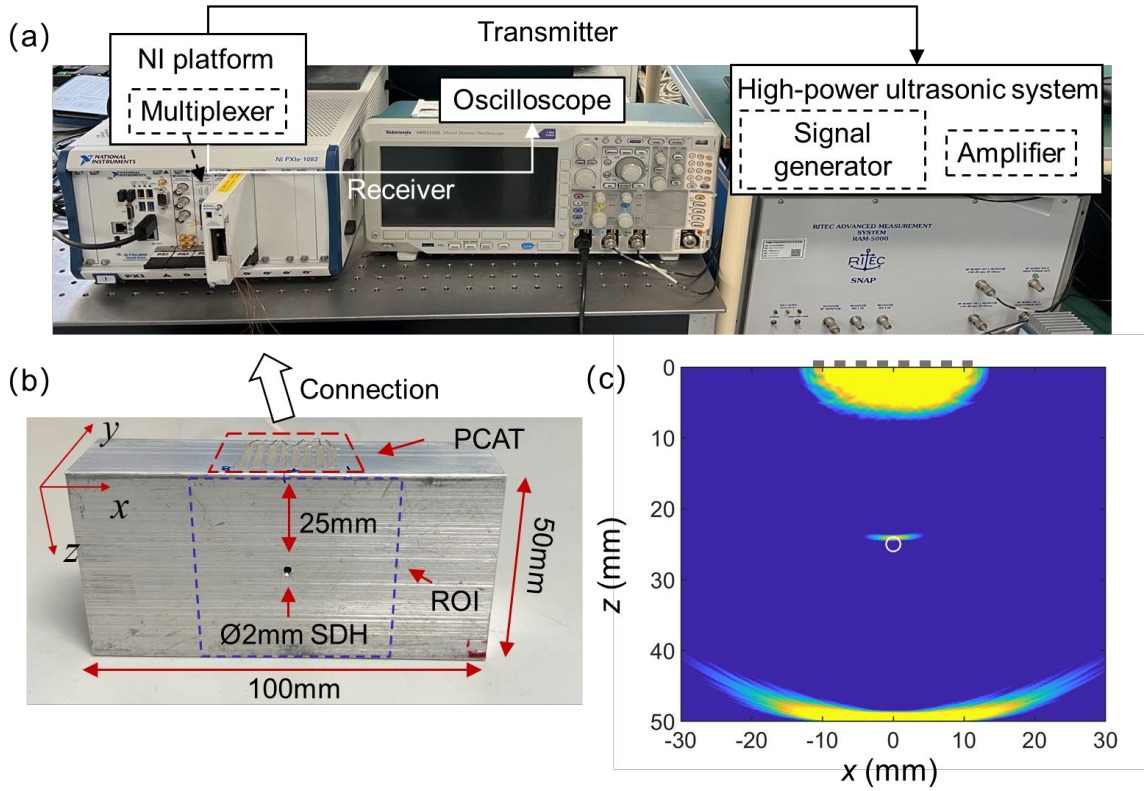

Figure 6. (a) Experimental setups of local monitoring with PCATs for internal defect imaging; (b) sample block with a flat surface; (c) experimental TFM image.

3.3.3 Applications on complex surfaces

To further evaluate the local monitoring performance of PCATs on complex surfaces, an aluminum block with a wavy upper surface was prepared as shown in **Figure 7a**. Two ROIs were selected for inspection, one with a concave surface and another with a convex surface. PCATs were conformally fabricated on the complex surface to detect the SDH within each ROI. The array parameters and operating excitation were the same as those used for the specimen with a flat surface, *i.e.*, 8-element PCAT and 2-cycle Hanning-windowed

sinusoidal tonebursts at 3MHz. Typical results of the transmitter-receiver path T_4R_6 are plotted in **Figure 7b**. Compared to the natural diverging wavefield of the concave surface, the defect reflection is more significant due to the natural focusing wavefield of the convex surface, not only in the absolute amplitude, but also in the relative ratio to the reflection of the bottom boundary (74.5% *vs.* 49.3%). Thus, better imaging performance can be obtained with less conspicuous artefacts caused by inter-element interference and bottom reflection, as shown in **Figure 7c** and **7d**.

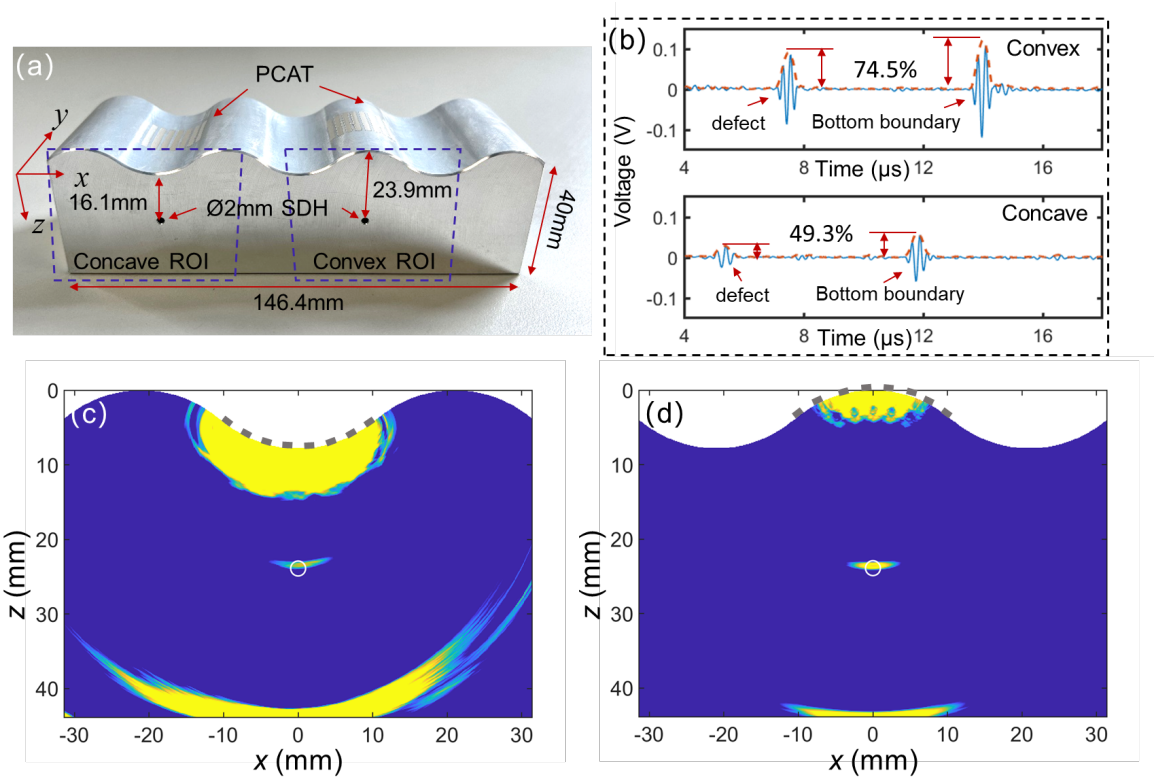

Figure 7. (a) Sample block with a wavy upper surface; (b) captured signals of the transmitter-receiver path T_4R_6 of convex ROI and concave ROI with envelope curves (orange dashed line); (c) experimental TFM image of concave ROI; (d) experimental TFM image of convex ROI.

4. Local Monitoring using Local Ultrasonic Resonances in Thin Structures

4.1. Principles and methods

The theory of elastic waves propagating on plates should be recalled first [3, 21]. For isotropic materials with a thickness of $h=2d$, the typical solutions can be derived from the

dispersion equation:

$$\frac{\tan qd}{\tan pd} = -\left[\frac{4k^2 pq}{\left(q^2 - k^2\right)^2}\right]^{\pm 1}, \quad \textbf{(5)}$$

where

$$p^2 = \frac{\omega^2}{C_L^2} - k^2, q^2 = \frac{\omega^2}{C_T^2} - k^2.$$

The exponent +1 is for symmetric and -1 for antisymmetric modes. ω is the circular frequency and frequency f equals $\omega/2\pi$. k is the eigenvalue which can be solved numerically as $\xi_{S_0}, \xi_{S_1}, \xi_{S_2}$... and $\xi_{A_0}, \xi_{A_1}, \xi_{A_2}$..., corresponding to wavenumbers of the symmetric modes and antisymmetric modes. The wavelength λ equals $2\pi/k$. Local resonances indicate that the energy is locally trapped in the source area without any transfer to the adjacent medium, *i.e.*, the energy or group velocity vanishes as

$$C_G = \frac{d\omega}{dk} = 0. \quad \textbf{(6)}$$

By solving **Equation 5** and **6** together, multiple local resonance modes can be obtained as shown in **Figure 8**. ZGV Lamb modes represent points (f_{ZGV}) on dispersion curves separating forward and backward propagating Lamb waves where k is nonzero and C_G vanishes (red dashed circles in **Figure 8**). For other modes, C_G vanishes with $k=0$ (*i.e.*, infinite λ), giving rise to thickness vibrations at the cut-off frequencies (f_{co}) of high-order Lamb modes associated with either the longitudinal (C_L) or shear (C_T) bulk wave in the plate thickness direction. Solutions of these thickness vibrations can be expressed according to their corresponding symmetric or antisymmetric Lamb modes, *i.e.,* thickness-stretch vibration modes (modes S_{2m+1} or A_{2n}) and thickness-shear vibration modes (modes S_{2n} and A_{2m+1}), as

$$\text{Symmetric modes}\begin{cases} S_{2n}: f_{co}\cdot h = nC_T \\ S_{2m+1}: f_{co}\cdot h = \dfrac{2m+1}{2}C_L \end{cases},\qquad \text{Antisymmetric modes}\begin{cases} A_{2n}: f_{co}\cdot h = nC_L \\ A_{2m+1}: f_{co}\cdot h = \dfrac{2m+1}{2}C_T \end{cases} \tag{7}$$

where $n \geq 1$ and $m \geq 0$. The order of thickness vibration modes is numbered according to the number of nodes present in the thickness of the plate (even or odd). It should be noted that in this study the Lamb modes are numbered consistent with their corresponding thickness vibration modes at cut-off frequencies, not the order of appearance in dispersion curves usually. All the ZGV Lamb wave modes and thickness vibration modes comprise the spectroscopy with high sensitivity to local mechanical properties.

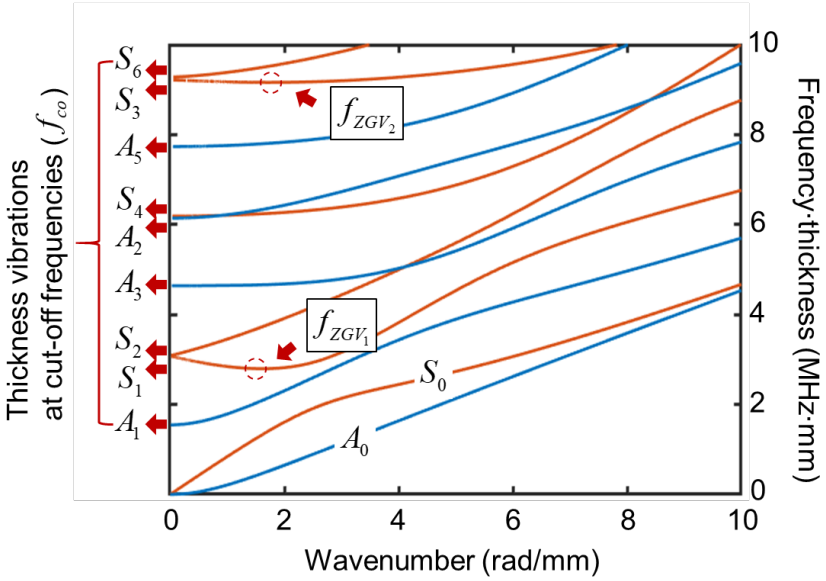

Figure 8. Dispersion curves of aluminum with multiple local resonance modes.

For a long time, contact transducers are not preferred to generate and detect local ultrasonic resonances since their rigidity and thickness would alter the local mechanical properties. PCATs have been proven to exhibit neglected influence on the propagating wavefield in the middle of the path due to ultra-thin thickness and low stiffness [34], which should also be valid on local resonances of covered structures. Moreover, the broad bandwidth and flat response of non-resonant PCATs ensure the robustness of this method by facilitating the

capture of multiple frequency peaks and their changes over a wide frequency range. As illustrated in **Figure 9**, PCATs are *in-situ* conformally fabricated on the surface of the hotspot region of the thin plate where damages through the thickness direction (z) are prone to initiate. In order to eliminate the influence of propagating waves on the measurement of local resonances, Individual element is used as a transmitter and receiver to monitor the local area (pulse-echo). Alternatively, paired elements (inter-element distance less than the ZGV wavelength) can be used as the transmitter and the receiver respectively (pitch-catch). The resonance analysis is conducted in the frequency spectrum through the fast Fourier transform (FFT) of measured time-series signals. Once the local resonances in the healthy status are recorded as the baseline, any shift or disappearance of these frequency peaks would be associated with local defects. If one or several resonance modes can be identified, quantification of defects could be achieved by their direct correlation with local thickness and stiffness (wave velocities).

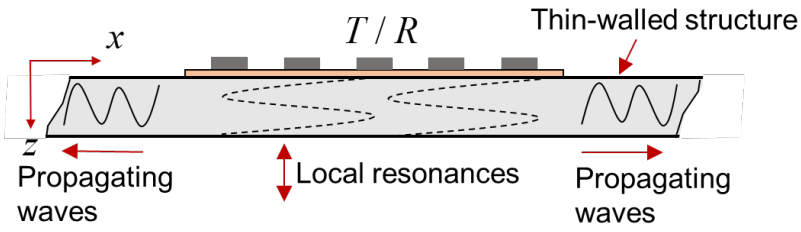

Figure 9. Schematics of local ultrasonic resonance-based local monitoring with PCATs.

4.2. Generation and detection of local resonances

4.2.1 Experimental setups

The generation of local resonances with PCATs was first investigated experimentally. As illustrated in **Figure 10**, a single PCAT element (18mm×2mm) was fabricated on one side surface of a thin aluminum plate (50mm×50mm) with a thickness h of 1mm. The large aspect ratio was selected to conform to the 2D assumption of plane waves. The width was selected as twice the plate thickness as the approximately optimal conditions for generating ZGV

Lamb wave modes of common metal materials (considering the elasticity was uncertain) [48], *i.e.,* approximately matching the half wavelength, while no certain requirement of source sizes for thickness vibration modes due to the infinite wavelength. An LDV was used to measure the out-of-plane velocity on the other side surface with increasing lateral distance (scanning from -8mm to 8mm in *x* direction, involving the PCAT-covered region) at the step of 0.25mm, with respect to the middle plane. The broadband excitation was a negative spike pulse emitted by JSR DPR300 Pulser/Receiver. For comparison, a piezoceramic strip (PZT-5H) with dimensions of 18mm×2mm×0.2mm and a pulsed laser source (Merion C, Quantel laser by LUMIBIRD) with a spot diameter focused to ~2mm were used to generate local resonances on one side surface of a same plate, respectively, of which the out-of-plane velocity on the other side surface was similarly detected by the lateral scanning LDV.

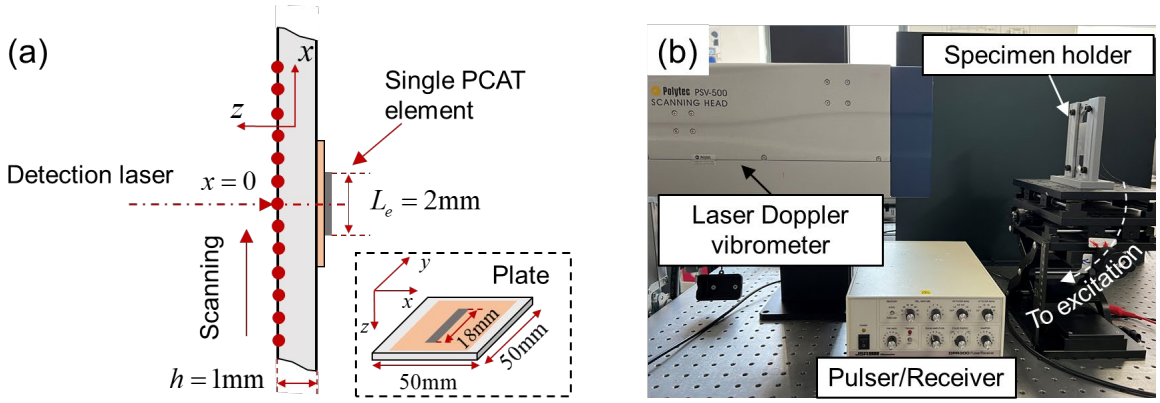

Figure 10. (a) Verification of local resonances generated by a single PCAT element; (b) experimental setups.

4.2.2 Results and discussions

With the measured ultrasonic signals at each point, the spatial-frequency spectrum can be obtained via 1D FFT. As shown in **Figure 11a** and **c**, apparent multi-mode local resonances within a broad frequency range (from 0-25MHz) can be observed with maximum values around the center point of the PCAT and laser source. However, the frequency band of PZT-generated signals is concentrated in the low-frequency range (from 0-10MHz) with disordered patterns in **Figure 11b**. This is probably due to the strong coupling between the

PZT layer and the host thin plate, which induces a complicated piezoelectric layered system in the local region and also involves axial and flexural vibration modes. Thus, the generated local resonances are difficult to interpret by physical modeling, as in EMI studies, where statistic methods are more favored.

Since the local resonance measurement with laser generation and laser detection has been well studied, three dominated ZGV Lamb modes within 0-25MHz can be easily identified in the frequency spectrum at the center point as shown in **Figure 11d**. While the relatively weaker thickness vibration modes are difficult to confirm due to the approaching of adjacent thickness-stretch and thickness-shear modes at cut-off frequencies, except A_3 which is separated from others. Interestingly, the spatial-frequency spectrum of PCAT generation is not the same as that of laser generation, mainly due to the different mode excitability and radiated wavefields caused by different coupling mechanisms, *i.e.*, the normal-pressure model of PCAT generation and the thermo-elastic model of laser generation. To achieve a better understanding of the generated local resonances, the experimental dispersion curves were achieved by the wavenumber-frequency spectrum via 2D FFT of ultrasonic signals along the propagating wave direction for PCAT and PZT generation. Due to the weak high-order propagating Lamb waves and overlapping of too many modes which make high-frequency experimental dispersion curves difficult to interpret, a low-frequency range with fewer modes existing was chosen for further investigation. The excitation was concentrated to this range using a monocycle sinusoidal toneburst with a center frequency of 3MHz.

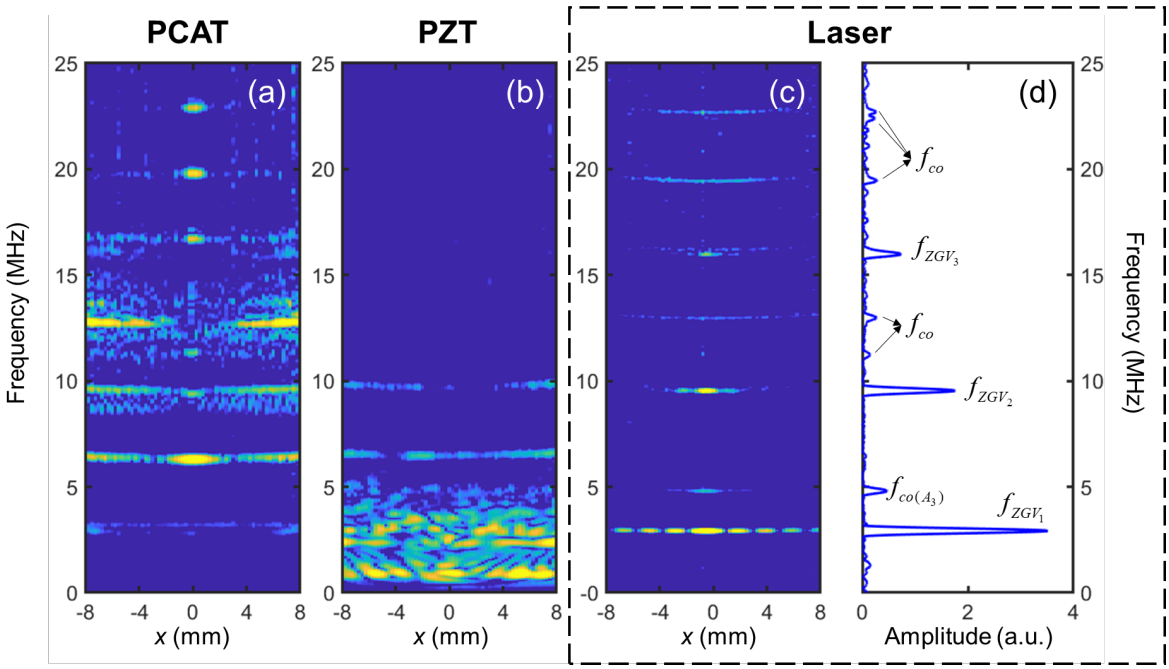

Figure 11. Spatial-frequency spectra of local resonances generated by (a) PCAT, (b) PZT, and (c) Laser; (d) frequency spectrum of laser-generated local resonances at the center point.

As shown in **Figure 12a** and **Figure 13a**, the experimental dispersion curves of propagating wavefields are in good agreement with the theoretical dispersion curves of the host thin plate for both PZT and PCAT generation. For the local resonances generated by PZT in **Figure 12b**, multiple peaks appear at low frequencies (red dashed rectangle) but cannot correspond to local resonance modes of the host thin plate in dispersion curves, which verified the dominated complex system in the local region. For the local resonances generated by the PCAT in **Figure 13b**, the three peaks of the frequency spectrum at the center point can correspond to the 1st ZGV point and the cut-off frequencies of two thickness vibration modes in dispersion curves. Thickness-shear modes A_1, A_3, and A_5 are not presented in the frequency spectrum, because the normal-pressure excitation generated by the PCAT on the host thin plate does not match the mode shapes of shear wave oscillation on the surface. Therefore, it is reasonable to grant the latter two frequency peaks to thickness-stretch modes S_1 and A_2 respectively, although they are entangled with thickness-shear modes S_2 and S_4. The smaller amplitude of mode S_1 could be due to the more radiated wavefields at lower frequencies which are also more deviated from the resonant frequency of PCAT. The 1st ZGV Lamb

mode can be generated due to the mode shape of which has both significant normal and lateral components on the surface. Unlike the dominated ZGV Lamb modes of local resonances by laser generation, the ZGV Lamb mode is small in the local resonances by PCAT generation probably due to the lower efficiency by normal-pressure excitation. Nevertheless, the two types of resonance modes successfully generated by the PCAT would benefit the defect quantification and expand the local monitoring applications, *e.g.*, inversion of elastic constants is possible with both longitudinal and shear wave velocities derived. Although not the focus of this study, these results also suggest the limitation of material characterization by fitting experimental dispersion curves obtained from long-distance scanning, which is not sensitive to local changes.

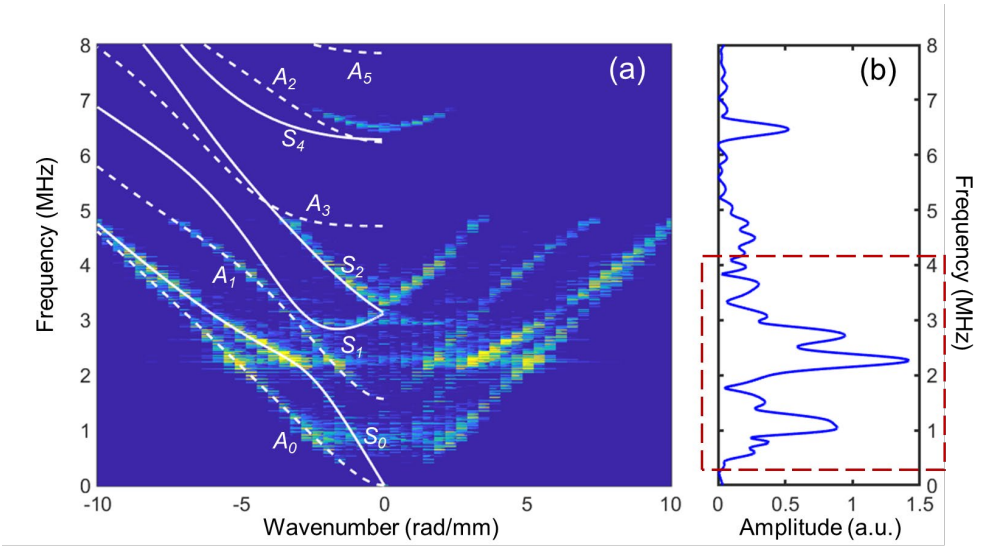

Figure 12. (a) Wavenumber-frequency spectrum of PZT-generated wavefield with theoretical dispersion curves (white lines); (b) frequency spectrum of PZT-generated local resonances at the center point.

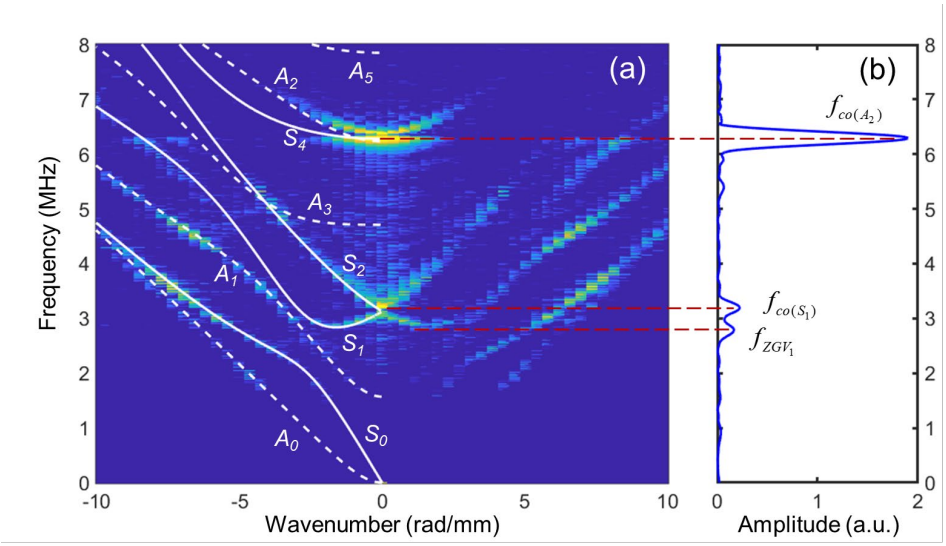

Figure 13. (a) Wavenumber-frequency spectrum of PCAT-generated wavefield with theoretical dispersion curves (white lines); (b) frequency spectrum of PCAT-generated local resonances at the center point.

To complete the measurement of local ultrasonic resonances, the detection by LDV was replaced with PCATs. Two measurement modes were investigated: (a) pulse-echo operation with a single PCAT element for transmitting and receiving by a diplexer; (b) pitch-catch operation with two elements of PCATs with a gap of 1mm as either transmitter or receiver separately. The results are listed in **Table 3**. Compared to the theoretic values, experimental results are different probably due to the uncertainty of elastic properties of specimens. The all-laser measurement was implemented on another plate, which could have a slightly different local thickness. Among PCAT generation with different detection techniques, LDV has the smallest detection aperture (spot diameter of ~60μm) and can be treated as the reference. The measuring error with PCAT detection should consider the spatial averaging effect of the element-covered area and/or the inter-element distance if paired elements are used. Nevertheless, these measuring errors should not be a problem for local monitoring, because a baseline could always be used by calibration of the healthy status. It should be noted that other peaks that appear at higher frequencies (>8MHz) in **Figure 11a** should be attributed to high-order modes and their strong amplitudes and narrow spans in *x* direction could be due to the convolution of the response and excitation near the resonant frequency

of PCAT and directional wavefields emitted by PCAT at high frequencies. Although not necessary to be used, these modes can also work as anchors in the baseline to improve the robustness of damage detection. The application of disbond defects in a multilayer structure with PCAT measurement of local ultrasonic resonances can be referred to the authors' previous work [49].

Table 3
Local ultrasonic resonance measurement of a 1mm aluminum plate.

Generation-Detection	Local ultrasonic resonances		
	f_{ZGV_1}	$f_{co(S_1)}$	$f_{co(A_2)}$
Theory	2.838	3.112	6.235
Pulsed laser-LDV	2.924	/	/
PCAT-LDV	2.777 (ref)	3.195 (ref)	6.293 (ref)
PCAT-PCAT(pulse-echo)	2.804 (9.63%)	3.199 (1.25%)	6.314 (3.34%)
PCAT-PCAT(pitch-catch)	2.796 (6.84%)	3.207 (3.76%)	6.344 (8.10%)

5. Concluding Remarks

In this study, the simple and conformal PCAT design by *in-situ* additive manufacturing has been greatly exploited in the field of SHM. Lightweight, low-profile, and flexible SHM networks can be straightforwardly applied on both developable and non-developable complex surfaces with high-production efficiency, high consistency, and adhesive-free installation. Besides its capability for Lamb wave-based large-area monitoring with mode tunability, PCAT realizes its potential for high-sensitivity, quantitative, and good-conformability local monitoring in critical hotspots of complex structures. Thanks to the normal-pressure coupling mechanism with host structures, PCAT can be combined with ultrasonic array inspection which has been well developed in the ultrasonic NDT field with bulk waves. Moreover, the broadband operating frequency and customizable electrode design enable it to be applicable to meet various local monitoring requirements in industrial scenarios. Optimization of array parameters for the sparse array design can be realized by

simulation tools, to achieve a balance between “sensing cost” and “sensing effectiveness” for real-time and on-board SHM purposes. The typical TFM algorithm was successfully used for internal defect imaging with PCATs applied on flat, concave, and convex surfaces of inspected specimens. Local ultrasonic resonance spectroscopy is another investigated method that can be implemented by single or paired PCAT elements for thin-walled or multilayer structures. With little disturbance to local mechanical properties, the multimodal resonances generated and detected can directly correspond to the ZGV Lamb wave modes and thickness vibration modes of host structures below, comparable to noncontact laser generation and detection. The broadband response ensures the successful capture of multiple peaks and their changes over a wide range in the frequency domain.

The versatility of PCAT creates an opportunity to exclusively build up multifunctional SHM networks. Hybrid damage information can be obtained by multi-scale complementary monitoring strategies, *i.e.,* large-area monitoring in in-plane direction using ultrasonic Lamb waves at tens to hundreds kHz in ordinary flat regions and high-sensitivity local monitoring in thickness direction using ultrasonic bulk waves and resonances at several to tens MHz only in critical featured regions. It should be mentioned that PZT networks have been well developed by integrating Lamb wave-based large-area monitoring and EMI-based local monitoring. However, the high-sensitive quantification of defect is difficult to achieve with EMI and an additional impedance measurement system is required. It should be noted that although the acquired ultrasonic data are limited in quality compared to current sophisticated NDT transducers, the cost of raw material and straightforward manufacture is less than 10 USD per PCAT, which facilitates the capability of a large volume permanent installation. Moreover, the introduction of advanced NDT technologies to the SHM field via PCAT offers great possibilities to further improve the currently proposed paradigms and will be

investigated in the author's future work. For example, 1D linear arrays could be extended to 2D planar arrays for 3D image reconstruction of damage; higher sensitivity could be achieved by reducing the pitch and increasing operating frequency; imaging quality could be improved with more advanced algorithms. As proof of concept, the proposed local monitoring methods were verified on aluminum specimens in this study. The extensions to more complex materials and realistic defects are under investigation, such as fiber-reinforced composites with delamination, metal structures with fatigue cracks or corrosion, and polymer-based materials with stiffness degradation. The applications of PCAT networks on realistic complex structures like airframes with an integrated scheme of large-area and local monitoring are also under investigation.

Declaration of Competing Interest

The authors declare that they have no known competing financial interests or personal relationships that could have appeared to influence the work reported in this paper.

Acknowledgments

This project is supported in part by the National Natural Science Foundation of China (Grant Nos. 52005493 and U2133213), in part by the Guangdong Basic and Applied Basic Research Foundation (Grant No. 2023A1515011190), in part by the Aeronautical Science Foundation of China (Grant No. 2022Z061133001), in part by the Department of Science and Technology of Guangdong Province (Grant Nos. 2019QN01H430 and 2019TQ05Z654), in part by the Natural Science Foundation of Guangdong Province (202381515040008), and in part by the Science and Technology Innovation Commission of Shenzhen (Grant Nos. ZDSYS20190902093209795, JCYJ20220818101215033, and JCYJ20180507182239617).

References

[1] P. Cawley, Structural health monitoring: Closing the gap between research and industrial deployment, Struct. Health Monit., 17 (2018) 1225-1244. https://doi.org/10.1177/1475921717750047

[2] A. Güemes, A. Fernandez-Lopez, A.R. Pozo, J. Sierra-Pérez, Structural Health Monitoring for Advanced Composite Structures: A Review, Journal of Composites Science, 2020. https://doi.org/10.3390/jcs4010013

[3] Z. Su, L. Ye, Identification of damage using Lamb waves: from fundamentals to applications, Springer Science & Business Media, 2009.

[4] X. Yang, K. Wang, P. Zhou, L. Xu, Z. Su, Imaging damage in plate waveguides using frequency-domain multiple signal classification (F-MUSIC), Ultrasonics, 119 (2022) 106607. https://doi.org/10.1016/j.ultras.2021.106607

[5] X. Qing, Y. Liao, Y. Wang, B. Chen, F. Zhang, Y. Wang, Machine Learning Based Quantitative Damage Monitoring of Composite Structure, International Journal of Smart and Nano Materials, 13 (2022) 167-202. 10.1080/19475411.2022.2054878

[6] C.C. Chia, S.Y. Lee, M.Y. Harmin, Y. Choi, J.-R. Lee, Guided ultrasonic waves propagation imaging: a review, Measurement Science and Technology, 34 (2023) 052001. https://doi.org/10.1088/1361-6501/acae27

[7] G. Franz, M.H. Hassan, Structural Health Monitoring of Laminated Materials for Aerospace Application, in: A.H. Ariffin, N.A. Latif, M.F.b. Mahmod, Z.B. Mohamad (Eds.) Structural Integrity and Monitoring for Composite Materials, Springer Nature Singapore, Singapore, 2023, pp. 1-26.

[8] D. Roach, Real time crack detection using mountable comparative vacuum monitoring sensors, Smart Structures and Systems, 5 (2009) 317-328. https://doi.org/10.12989/SSS.2009.5.4.317

[9] Y.-K. An, H. Sohn, Integrated impedance and guided wave based damage detection, Mech. Syst. Signal Pr., 28 (2012) 50-62. https://doi.org/10.1016/j.ymssp.2011.11.016

[10] D. Wang, J. He, B. Dong, X. Liu, W. Zhang, Novel Damage Detection Techniques for Structural Health Monitoring Using a Hybrid Sensor, Math Probl Eng, 2016 (2016) 3734258. https://doi.org/10.1155/2016/3734258

[11] B.W. Drinkwater, P.D. Wilcox, Ultrasonic arrays for non-destructive evaluation: A review, NDT&E Int., 39 (2006) 525-541. https://doi.org/10.1016/j.ndteint.2006.03.006

[12] Z. Zhang, Q. Li, A. Cao, W. Yeoh, M. Liu, W. Yang, Defect identification in thick porous and wavy composites with hybrid use of ultrasound non-reciprocity and scattering, Compos. Sci. Technol. , 225 (2022) 109514. https://doi.org/10.1016/j.compscitech.2022.109514

[13] K.J. Langenberg, M. Berger, T. Kreutter, K. Mayer, V. Schmitz, Synthetic aperture focusing technique signal processing, NDT International, 19 (1986) 177-189. https://doi.org/10.1016/0308-9126(86)90107-0

[14] J. Tian, M. Liu, H. Xiao, Z. Zhang, W. Yang, Z. Long, C. Ming Leung, Optimized ultrasonic total focusing imaging of diverse and multiple defects in crossply CFRP: Floquet wave theory, numerical simulation, and experimental validation, Mech. Syst. Signal Pr., 199 (2023) 110486. https://doi.org/10.1016/j.ymssp.2023.110486

[15] C. Holmes, B.W. Drinkwater, P.D. Wilcox, Post-processing of the full matrix of ultrasonic transmit–receive array data for non-destructive evaluation, NDT&E Int., 38 (2005) 701-711. https://doi.org/10.1016/j.ndteint.2005.04.002

[16] J.M. Cannata, J.A. Williams, Z. Qifa, T.A. Ritter, K.K. Shung, Development of a 35-MHz piezo-composite ultrasound array for medical imaging, IEEE Trans. Ultrason. Ferroelectr. Freq. Control, 53 (2006) 224-236. https://doi.org/10.1109/TUFFC.2006.1588408

[17] K. Kimura, H. Ohigashi, Generation of very high‐frequency ultrasonic waves using thin films of vinylidene fluoride‐trifluoroethylene copolymer, J. Appl. Phys. , 61 (1987) 4749-4754. https://doi.org/10.1063/1.338812

[18] Y. Li, K. Wang, Q. Wang, J. Yang, P. Zhou, Y. Su, S. Guo, Z. Su, Acousto-ultrasonics-based health monitoring for nano-engineered composites using a dispersive graphene-networked sensing system, Struct. Health Monit., 20 (2020) 240-254. https://doi.org/10.1177/1475921720929749

[19] Z. Zeng, M. Liu, H. Xu, Y. Liao, F. Duan, L.-m. Zhou, H. Jin, Z. Zhang, Z. Su, Ultra-broadband frequency responsive sensor based on lightweight and flexible carbon nanostructured polymeric nanocomposites, Carbon, 121 (2017) 490-501. https://doi.org/10.1016/j.carbon.2017.06.011

[20] H. Ren, X. Yang, Z. Wang, X. Xu, R. Wang, Q. Ge, Y. Xiong, Smart structures with embedded flexible sensors fabricated by fused deposition modeling-based multimaterial 3D printing, International Journal of Smart and Nano Materials, 13 (2022) 447-464. 10.1080/19475411.2022.2095454

[21] V. Giurgiutiu, Structural Health Monitoring with Piezoelectric Wafer Active Sensors, 2nd ed., Academic Press, 2014.

[22] Y. Wang, L. Qiu, Y. Luo, R. Ding, F. Jiang, A piezoelectric sensor network with shared signal transmission wires for structural health monitoring of aircraft smart skin, Mech. Syst. Signal Pr., 141 (2020) 106730. https://doi.org/10.1016/j.ymssp.2020.106730

[23] X.P. Qing, S.J. Beard, A. Kumar, I. Li, M. Lin, F.-K. Chang, Stanford Multiactuator–Receiver Transduction (SMART) Layer Technology and Its Applications, Encyclopedia of Structural Health Monitoring, 2009.

[24] X. Sun, A.J. Croxford, B.W. Drinkwater, Continuous monitoring with a permanently installed high-resolution ultrasonic phased array, Struct. Health Monit., 0 (2023) 14759217231152413. https://doi.org/10.1177/14759217231152413

[25] H. Hu, X. Zhu, C. Wang, L. Zhang, X. Li, S. Lee, Z. Huang, R. Chen, Z. Chen, C. Wang, Y. Gu, Y. Chen, Y. Lei, T. Zhang, N. Kim, Y. Guo, Y. Teng, W. Zhou, Y. Li, A. Nomoto, S. Sternini, Q. Zhou, M. Pharr, F.L. di Scalea, S. Xu, Stretchable ultrasonic transducer arrays for three-dimensional

imaging on complex surfaces, Sci. Adv., 4 (2018) eaar3979. https://doi.org/10.1126/sciadv.aar3979
[26] G. Watzl, C. Kerschbaummayr, M. Schagerl, T. Mitter, B. Sonderegger, C. Grünsteidl, In situ laser-ultrasonic monitoring of Poisson's ratio and bulk sound velocities of steel plates during thermal processes, Acta Mater. , 235 (2022) 118097. https://doi.org/10.1016/j.actamat.2022.118097
[27] R. Hodé, S. Raetz, J. Blondeau, N. Chigarev, N. Cuvillier, V. Tournat, M. Ducousso, Nondestructive evaluation of structural adhesive bonding using the attenuation of zero-group-velocity Lamb modes, Appl. Phys. Lett. , 116 (2020). https://doi.org/10.1063/1.5143215
[28] C. Grünsteidl, T. Berer, M. Hettich, I. Veres, Determination of thickness and bulk sound velocities of isotropic plates using zero-group-velocity Lamb waves, Appl. Phys. Lett. , 112 (2018). https://doi.org/10.1063/1.5034313
[29] C. Prada, D. Clorennec, D. Royer, Local vibration of an elastic plate and zero-group velocity Lamb modes, The Journal of the Acoustical Society of America, 124 (2008) 203-212. https://doi.org/10.1121/1.2918543
[30] Q. Xie, S. Mezil, P.H. Otsuka, M. Tomoda, J. Laurent, O. Matsuda, Z. Shen, O.B. Wright, Imaging gigahertz zero-group-velocity Lamb waves, Nature Communications, 10 (2019) 2228. https://doi.org/10.1038/s41467-019-10085-4
[31] S. Dixon, C. Edwards, S.B. Palmer, High accuracy non-contact ultrasonic thickness gauging of aluminium sheet using electromagnetic acoustic transducers, Ultrasonics, 39 (2001) 445-453. https://doi.org/10.1016/S0041-624X(01)00083-X
[32] S.D. Holland, D.E. Chimenti, High contrast air-coupled acoustic imaging with zero group velocity lamb modes, Ultrasonics, 42 (2004) 957-960. https://doi.org/10.1016/j.ultras.2003.12.009
[33] S. Park, C.B. Yun, D.J. Inman, Structural health monitoring using electro-mechanical impedance sensors, Fatigue Fract Eng M, 31 (2008) 714-724. https://doi.org/10.1111/j.1460-2695.2008.01248.x
[34] Y. Li, W. Feng, L. Meng, K.M. Tse, Z. Li, L. Huang, Z. Su, S. Guo, Investigation on in-situ sprayed, annealed and corona poled PVDF-TrFE coatings for guided wave-based structural health monitoring: From crystallization to piezoelectricity, Materials & Design, 199 (2021) 109415. https://doi.org/10.1016/j.matdes.2020.109415
[35] Y. Li, K. Wang, W. Feng, H. Wu, Z. Su, S. Guo, Insight into excitation and acquisition mechanism and mode control of Lamb waves with piezopolymer coating-based array transducers: Analytical and experimental analysis, Mech. Syst. Signal Pr., 178 (2022) 109330. https://doi.org/10.1016/j.ymssp.2022.109330
[36] T.d.A. Prado, H.L. Moura, T.A.R. Passarin, G.A. Guarneri, G.P. Pires, D.R. Pipa, A straightforward method to evaluate the directivity function of ultrasound imaging systems, NDT&E Int., 119 (2021) 102402. https://doi.org/10.1016/j.ndteint.2021.102402
[37] P.D. Wilcox, J. Zhang, Quantification of the Effect of Array Element Pitch on Imaging Performance, IEEE Trans. Ultrason. Ferroelectr. Freq. Control, 65 (2018) 600-616. https://doi.org/10.1109/TUFFC.2018.2794627

[38] H. He, K. Sun, C. Sun, J. He, E. Liang, Q. Liu, Suppressing artifacts in the total focusing method using the directivity of laser ultrasound, Photoacoustics, 31 (2023) 100490. https://doi.org/10.1016/j.pacs.2023.100490

[39] J. Song, Y. Liu, S. Ma, Ultrasonic phased array sparse-TFM imaging based on deep learning and genetic algorithm, Proc. SPIE12076, 2021 International Conference on Image, Video Processing, and Artificial Intelligence, 1207606 (2021). https://doi.org/10.1117/12.2607915

[40] H. Hu, J. Du, C. Ye, X. Li, Ultrasonic Phased Array Sparse-TFM Imaging Based on Sparse Array Optimization and New Edge-Directed Interpolation, Sensors, 2018. https://doi.org/10.3390/s18061830

[41] X. Sun, A.J. Croxford, B.W. Drinkwater, Rapid ultrasonic array assessment framework method for evaluating ultrasonic array transducer performance, Appl Acoust, 182 (2021) 108246. https://doi.org/10.1016/j.apacoust.2021.108246

[42] A.A. Kurnikov, K.G. Pavlova, A.G. Orlova, A.V. Khilov, V.V. Perekatova, A.V. Kovalchuk, P.V. Subochev, Broadband (100 kHz – 100 MHz) ultrasound PVDF detectors for raster-scan optoacoustic angiography with acoustic resolution, Quantum Electron. , 51 (2021) 383. https://doi.org/10.1070/QEL17538

[43] J.M. Allin, P. Cawley, Design and construction of a low frequency wide band non-resonant transducer, Ultrasonics, 41 (2003) 147-155. https://doi.org/10.1016/S0041-624X(03)00102-1

[44] V. Devaraju, P.A. Lewin, P.E. Bloomfield, Development of non-resonant transducers for ultrasound imaging, Proceedings of the IEEE 28th Annual Northeast Bioengineering Conference (IEEE Cat. No.02CH37342), 2002, pp. 245-246. https://doi.org/10.1109/NEBC.2002.999557

[45] P.A. Lewin, Q. Zhang, Nonresonant transducers for ultrasound imaging, Journal of the Acoustical Society of Japan (E), 18 (1997) 215-222. https://doi.org/10.1250/ast.18.215

[46] V.V. Yakovlev, W. Dickson, A. Murphy, J. McPhillips, R.J. Pollard, V.A. Podolskiy, A.V. Zayats, Ultrasensitive Non-Resonant Detection of Ultrasound with Plasmonic Metamaterials, Adv. Mater. , 25 (2013) 2351-2356. https://doi.org/10.1002/adma.201300314

[47] D.L. E, Laser ultrasonics techniques and applications, Routledge, 1990.

[48] D. Clorennec, C. Prada, D. Royer, Local and noncontact measurements of bulk acoustic wave velocities in thin isotropic plates and shells using zero group velocity Lamb modes, J. Appl. Phys. , 101 (2007). https://doi.org/10.1063/1.2434824

[49] Q. Liu, Y. Li, R. Guan, J. Yan, M. Liu, G. Luo, Z. Su, X. Qing, K. Wang, Advancing measurement of zero-group-velocity Lamb waves using PVDF-TrFE transducers: first data and application to in situ health monitoring of multilayer bonded structures, Struct. Health Monit., 22 (2023) 2641-2650. https://doi.org/10.1177/14759217221126812